Controlled Growth of High-Quality Monolayer WS_2 Layers on Sapphire and Imaging Its Grain Boundary

Yu Zhang,[†,‡] Yanfeng Zhang,[†,‡,*] Qingqing Ji,[‡] Jing Ju,[§] Hongtao Yuan,[⊥,∥] Jianping Shi,[†] Teng Gao,[‡] Donglin Ma,[‡] Mengxi Liu,[‡] Yubin Chen,[‡] Xiuju Song,[†] Harold Y. Hwang,[⊥,∥] Yi Cui,[⊥,∥] and Zhongfan Liu[‡]

[†]Department of Materials Science and Engineering, College of Engineering, Peking University, Beijing 100871, People's Republic of China, [‡]Center for Nanochemistry (CNC), Beijing National Laboratory for Molecular Sciences, College of Chemistry and Molecular Engineering, Academy for Advanced Interdisciplinary Studies, Peking University, Beijing 100871, People's Republic of China, [§]State Key Laboratory of Rare Earth Materials Chemistry and Applications, College of Chemistry and Molecular Engineering, Peking University, Beijing 100871, People's Republic of China, [⊥]Geballe Laboratory for Advanced Materials, Stanford University, Stanford, California 94025, United States, and [∥]SLAC National Accelerator Laboratory, Stanford Institute for Materials and Energy Sciences, Menlo Park, California 94025, United States

ABSTRACT Atomically thin tungsten disulfide (WS_2), a structural analogue to MoS_2, has attracted great interest due to its indirect-to-direct band-gap tunability, giant spin splitting, and valley-related physics. However, the batch production of layered WS_2 is underdeveloped (as compared with that of MoS_2) for exploring these fundamental issues and developing its applications. Here, using a low-pressure chemical vapor deposition method, we demonstrate that high-crystalline mono- and few-layer WS_2 flakes and even complete layers can be synthesized on sapphire with the domain size exceeding 50 × 50 μm^2. Intriguingly, we show that, with adding minor H_2 carrier gas, the shape of monolayer WS_2 flakes can be tailored from jagged to straight edge triangles and still single crystalline. Meanwhile, some intersecting triangle shape flakes are concomitantly evolved from more than one nucleus to show a polycrystalline nature. It is interesting to see that, only through a mild sample oxidation process, the grain boundaries are easily recognizable by scanning electron microscopy due to its altered contrasts. Hereby, controlling the initial nucleation state is crucial for synthesizing large-scale single-crystalline flakes. We believe that this work would benefit the controlled growth of high-quality transition metal dichalcogenide, as well as in their future applications in nanoelectronics, optoelectronics, and solar energy conversions.

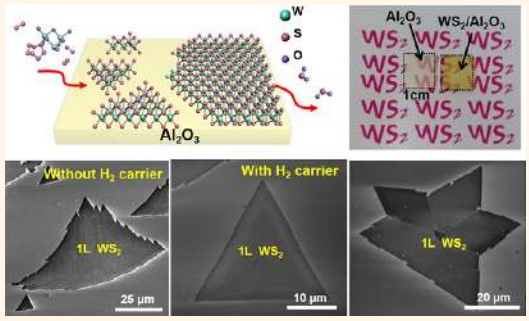

KEYWORDS: transition metal dichalcogenide · monolayer · domain boundary · thickness control · characterization

Atomically thin two-dimensional (2D) materials,[1,2] for example graphene,[3] have attracted great attention in recent years because of their abundant intriguing properties related to their lower dimensionality. Whereas the zero energy gap of graphene blocks its applications in logic electronics and field-effect transistors, semiconducting transition metal dichalcogenides (TMDCs),[4−6] such as MoS_2 and WS_2, have recently emerged as a new family of 2D materials, with electronic properties complementary to that of semimetallic graphene. Interest in such materials, in particular molybdenum disulfide (MoS_2), has increased exponentially due to its potential applications in 2D semiconductors with remarkable electronic and optical properties.[4]

Similar to MoS_2, WS_2 crystallizes in a van der Waals layered structure where each layer consists of a slab S−W−S sandwich. It possesses many similar characteristics to that of MoS_2, such as the indirect-to-direct band-gap transition in the monolayer regime,[7] coupled spin and valley physics,[8] and band structure tunability with strain.[9] Furthermore, the combination of WS_2 thin layers with other 2D materials has given rise to a large category of 2D heterostructures.[10−12]

Recently, the preparation of TMDC thin layers has caught much attention from the scientific community to fulfill a wide range of applications. WS_2 flakes have been obtained *via* mechanical exfoliation,[7,8,13] chemical exfoliation,[14,15] liquid exfoliation,[16,17] chemical synthesis,[18−20] and sulfurization of tungsten oxide films.[21,22] Nevertheless, in order to meet application needs in field-effect transistors (FET),[11,18,23] hydrogen evolution,[14] and optoelectronic devices,[4,24]

* Address correspondence to yanfengzhang@pku.edu.cn.

Received for review July 8, 2013 and accepted September 18, 2013.

Published online September 18, 2013
10.1021/nn403454e

the growth still needs to be improved in many aspects, for example, the domain size, crystal quality, and thickness controllability.

Here, we present the synthesis of single- and few-layer WS_2 triangular flakes on a new substrate of sapphire (Al_2O_3) *via* low-pressure chemical vapor deposition (LPCVD) reaction of WO_3 and sulfur. The size of single crystal domains was measured to be as large as ~50 μm. The coverage and thickness of WS_2 were controlled by adjusting the growth temperature or the source–substrate distance. The shape of the flakes was modified by adding H_2 carrier gas to the existing Ar gas flow. Raman spectroscopy, photoluminescence (PL), atomic force microscopy (AFM), scanning electron microscopy (SEM), and high-resolution transmission electron microscopy (HRTEM) were utilized to characterize the thickness, domain size, and the crystal quality of the WS_2 sample. Moreover, a portable mild oxidation process was also introduced to identify the domain boundary of joining or intersecting polycrystalline flakes. The transport properties of as-grown WS_2 flakes were also examined using ionic liquid gated devices.

RESULTS AND DISCUSSION

Figure 1a demonstrates the related chemical reaction of WS_2 growth on a sapphire substrate. Briefly, WO_3 was partially reduced by sulfur vapor to form volatile suboxide species WO_{3-x}, which is further sulfurized with the formation of WS_2 on sapphire:

$$7S + 2WO_3 \rightarrow 2WS_2 + 3SO_2 \quad (1)$$

A schematic illustration of the LPCVD apparatus is shown in Figure 1b. Sulfur powder was mildly sublimated at ~100 °C and carried by Ar (or in a mixture with H_2) gas flow to keep the subsequent growth zone in a sulfur-rich atmosphere. The WO_3 powder and Al_2O_3 substrates were heated to ~900 °C with the LPCVD system pumped down to ~30 Pa.

Figure 1c–e show the SEM morphologies of the as-grown WS_2 samples. The darker contrast regions are tentatively attributed to WS_2 and the regions around are the Al_2O_3 substrate. Under pure Ar carrier gas flow, asymmetrical triangular WS_2 flakes with jagged edges usually formed with an edge length exceeding 50 μm (Figure 1c and its zoom-in image Figure 1d). The (0001) plane of sapphire is hexagonally arranged (Figure S1), and coinciding with the symmetry of the WS_2 lattice, the asymmetry in the shape of the WS_2 flakes cannot be attributed to the lattice anisotropy of Al_2O_3 (0001) but probably mediated by a dynamic process.[25] The corresponding AFM image (Figure 1f) gives a flake height of ~0.8 nm, which agrees well with the reported thickness for monolayer WS_2.[21] Note that Figure 1e is typical of a rather small flake occasionally observed on the same surface possessing a relatively sharp edge.

Intriguingly, when the carrier gas was switched to mixed Ar and H_2 flow (8:1 in volume flow rate), nearly equilateral triangular and intersecting (or joining) triangular shaped monolayer WS_2 with straight edges could also be synthesized (Figure 1g–i). As it is known that H_2 is a more reductive reagent than sulfur, H_2 may directly promote WO_3 reduction, or H_2S formation to reduce WO_3, so as to make a more WO_{3-x}-rich environment for WS_2 growth,[26]

$$WO_3 + 3S + H_2 \rightarrow WS_2 + SO_2 + H_2O \quad (2)$$

The growth with H_2 is hence considered to be mediated by a kinetic effect, leading to the thermodynamically stable geometry of a regular triangular shape,[27] in agreement with published results[21,26,28,29] (see Supporting Information Figure S2). The triangular shaped flakes with sharp or crooked edges (Figure 1h,i) are expected to be W- or S-terminated ones, as previous works have reported a preferred zigzag-oriented edge for triangular CVD WS_2 flakes.[21,29–31]

It is noteworthy that, first, the monolayer WS_2 crystals prepared in this study possess a much larger domain size (~50 μm) compared to previous work with similar chemical synthesis methods (15 μm).[21,32] Second, the growth under a mixture of Ar and H_2 carrier gas usually results in a smaller flake size than that without H_2 (see Supporting Information Figure S3). Furthermore, the introduction of H_2 affects the flake shape in the growth process but does not modify its shape after growth (see Supporting Information Figure S4). Finally, by adjusting the distance between precursors and sapphire substrates, WS_2 films with a uniform thickness and high coverage ratio (~90%) can be prepared (see Supporting Information Figure S5). This is demonstrated by a photograph of such a sample (Figure 1j), exhibiting a nearly uniform, transparent, and earthy yellow color (with respect to the bare Al_2O_3 substrates) (for more details see Supporting Information Figure S6).

SEM and AFM measurements were then employed to systematically study the thickness distribution, correlation of shape and thickness with growth temperature, and source–substrate distance (D_{ss}), only with Ar as carrier gas. Note that the growth under mixed H_2 carrier also leads to the same high-quality WS_2 layers (see Supporting Information Figure S7). Figure 2a–c present several typical SEM morphologies of monolayer (1L), 1L, and 5L flakes, giving film thickness of ~0.8 nm, ~0.8 nm, and ~4.0 nm by AFM height profiles, respectively (Figure 2d–f; also see Figure S8).

At a growth temperature of 880 °C, the monolayer WS_2 flake (Figure 2a) usually shows a much rougher edge, probably due to a lower crystallinity. In contrast, under 900 °C growth, the flake boundaries present a sawtoothed shape (Figure 2b) corresponding to an improved film crystal quality. Meanwhile, the flake size of the monolayer WS_2 is dramatically increased up to ~50 μm upon increasing the growth temperature from 880 °C to 900 °C (Figure 2a,b). In order to explain this temperature effect, it is reasonable to infer that a

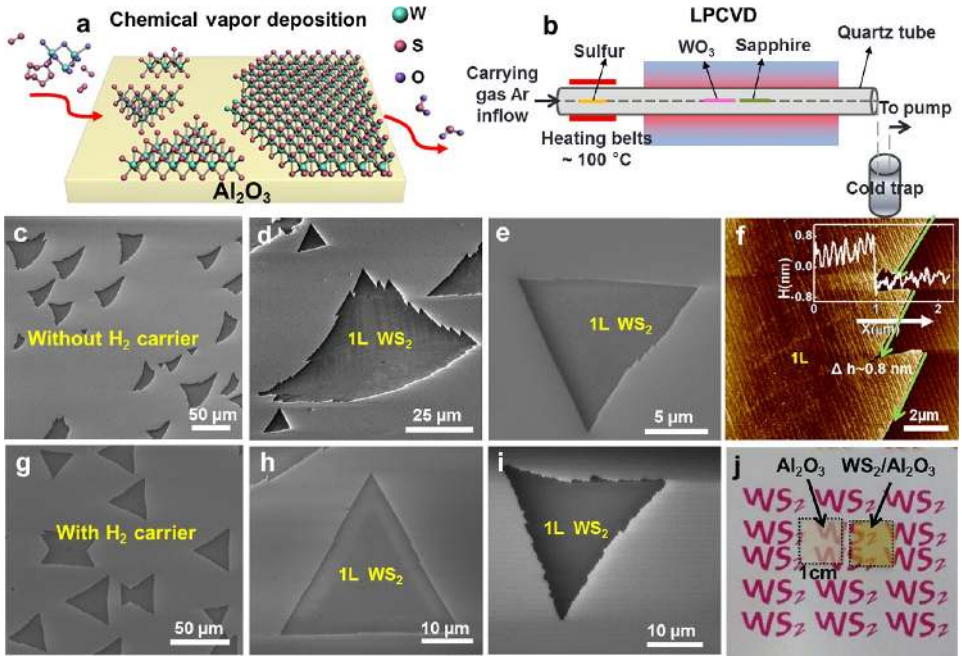

Figure 1. LPCVD synthesis of WS_2 on sapphire. (a) Schematic view of the related chemical reaction. (b) Experimental setup of the LPCVD system. (c, d, e) SEM images of jagged edge WS_2 flakes synthesized under pure Ar gas flow. (f) Corresponding AFM characterization of the monolayer nature. (g, h, i) SEM images of WS_2 flakes synthesized under mixed Ar and H_2 gas flow. (j) Photograph of bare sapphire and monolayer as-grown WS_2.

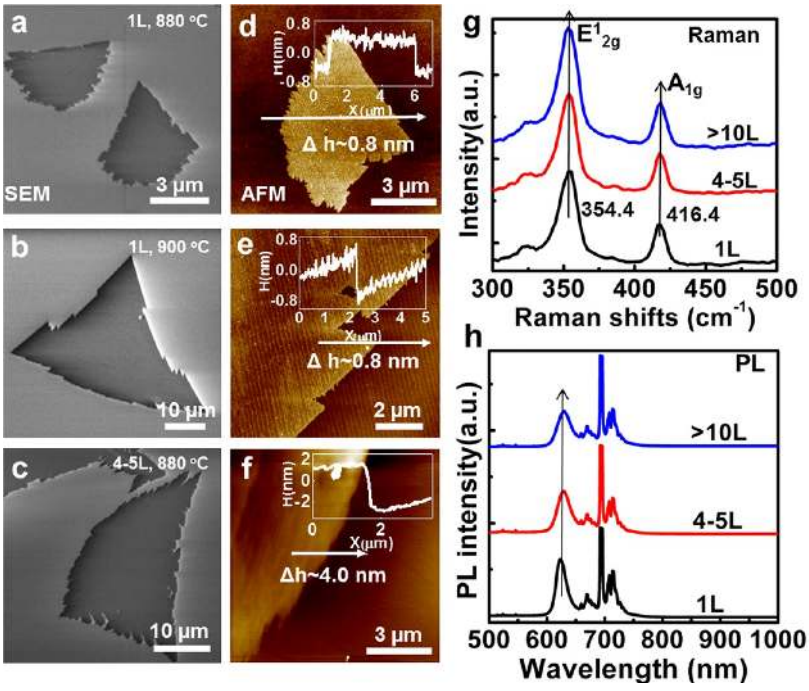

Figure 2. SEM, AFM, Raman, and PL properties of mono- and few-layer WS_2 flakes on sapphire. (a–c) SEM images of WS_2 flakes grown at 880 °C with a source–substrate distance (D_{ss}) of ~10 cm, at 900 °C with a D_{ss} of ~10 cm, and at 880 °C with a D_{ss} of ~9 cm, respectively. (d–f) Corresponding AFM images of as-grown WS_2 flakes in a–c, respectively. Line profiles along the white arrows are provided as insets. (g, h) Raman and PL spectra of as-grown WS_2 samples.

higher growth temperature restrains nucleation and deposition of WS_2 on the substrate, resulting in decreased nucleation density. Meanwhile, a higher growth temperature facilitates the surface diffusion of WO_3 and WO_{3-x}, as well as the reaction of WO_{3-x} with S, thus in line with better crystallization of WS_2 lattices and increased flake size.

It is also found that, in the same growth batch, the distance between the WO_3 precursor and Al_2O_3 substrate is also found to be an essential parameter in

determining the film thickness. Figure 2c shows few-layer WS_2 formation with D_{ss} ~9 cm at 880 °C, which is in contrast with monolayer formation with D_{ss} ~10 cm (Figure 2a) (also see Supporting Information Figure S5).

As a result, through careful control of the above growth parameters, high-quality and large-scale monolayer WS_2 can be synthesized even at a coverage of ~90%. The centimeter-scale monolayer sample may serve as a perfect candidate for exploring the unique electronic and optoelectronic properties. Moreover, the few-layer samples acquired through a single growth may serve as perfect candidates for probing thickness-dependent properties, considering its energy band tunability with thickness.

With the as-grown WS_2 samples at 900 °C, Raman measurements were also performed to determine the film thickness and the crystal quality. Figure 2g shows the E^1_{2g} and A_{1g} phonon modes of monolayer WS_2, which are located at 354.4 and 416.4 cm^{-1}, respectively. The E^1_{2g} phonon mode slightly red-shifts with increased layer number to 353.8 cm^{-1} for 4−5L and then 353.4 cm^{-1} for >10L, while the A_{1g} phonon mode shows a more evident blue-shift with increased thickness (417.3 cm^{-1} for 4−5L and 418.3 cm^{-1} for >10L, respectively, upper two spectra). Nevertheless, the frequency difference of the two modes (E^1_{2g} and A_{1g}) monotonically decreases with reduced film thickness, which coincides with previous reports for WS_2 on SiO_2/Si or other insulating substrates.[8,21] Consequently, the difference between A_{1g} and E^1_{2g} modes is still a key factor for thickness identification, although different substrates may induce a small shift of the specific vibration mode.

Figure 2h presents the PL spectra of monolayer and few-layer WS_2 samples (with 514 nm laser excitation), normalized by the intensity of the Raman E^1_{2g} peak, in order to rule out external effects such as laser power and local electric field effects. Interestingly, although measured directly on sapphire, the PL intensity of monolayer WS_2 is much stronger than that for a few layers, consistent with its direct-gap property. Furthermore, the PL characteristic peaks of WS_2 (at ~625 nm) are red-shifted with increasing layer thickness, which are located at 622.6, 628.3, and 629.1 nm for 1L, 4−5L, and >10L, respectively. These results illustrate an obvious intensity and position dependence of the PL characteristic peak. Note that emission from 600 to 800 nm wavelength should arise from the PL background signal from the sapphire substrate, which is indeed incorporated into the characteristic spectra of WS_2 (see Supporting Information Figure S9).

In this case, transference of WS_2 layers to other arbitrary substrates is highly useful. The transfer method is derived from the commonly used one by detaching the sapphire substrate with a concentrated NaOH solution. Figure 3a−c present the SEM images of as-grown and transferred monolayer WS_2 flakes (on SiO_2/Si) and its optical image, respectively. Similarly, Figure 3d−f show the SEM (on Al_2O_3), optical, and PL mapping (on SiO_2) images of a nearly whole coverage monolayer WS_2 film. In addition to the uniform OM contrasts, the nearly uniform PL mapping data confirm the large-scale uniformity of the thickness, considering that the PL yield significantly depends on layer thickness. Furthermore, the height profile measured along the film edge (~0.8 nm in height) confirms its monolayer nature (see Supporting Information Figure S6). Obviously, the LPCVD synthesized WS_2 sample on sapphire can be transferred intactly onto SiO_2/Si, which may facilitate its future applications.

Figure 3g,h exhibit the Raman and PL spectra of as-grown and transferred monolayer WS_2 flakes, respectively. The two characteristic Raman peaks have a minor shift after transfer (Figure 3g). Meanwhile, the peak width of the transferred sample becomes greater, probably arising from the charge inhomogeneity of SiO_2 substrates and lattice defects in WS_2 introduced from the transfer process. The difference of the E^1_{2g} (354.4 cm^{-1}) and A_{1g} (416.8 cm^{-1}) phonon modes ($\Delta\omega$ = 62.4 cm^{-1}) of the transferred sample agrees well with that of physically exfoliated and chemically synthesized monolayer WS_2,[7,21,22] again suggesting the monolayer nature of the synthesized WS_2 flakes. Importantly, the PL signal on SiO_2/Si is prominently enhanced compared to that on sapphire (Figure 3h). This may come from the weaker coupling of transferred WS_2 with SiO_2/Si than that of the as-grown sample on sapphire.

Raman and PL spectra of transferred monolayer and few-layer WS_2 were subsequently achieved (Figure 3i,j). The E^1_{2g} mode of Raman spectra presents a red-shift from monolayer to several layers, while the A_{1g} phonon mode shows almost no shift (Figure 3i). The PL peak also red-shifts when increasing the layer number from monolayer to several layers (Figure 3j). All these tendencies agree well with that of the nontransferred sample and the published results on exfoliated few-layer WS_2.[7,8] In this case, Raman and PL spectra of both as-grown and transferred WS_2 layers possess a clear thickness-dependent feature.

For the monolayer WS_2 flakes grown under mixed Ar and H_2 gas flow, many abnormal structures composed of intersecting or joining triangles (Figure 4a) were imaged as butterfly-like (Figure 4b) and star-like structures (Figures 4c,d), which is similar to the case of CVD MoS_2.[29] The sample can be stable in air for a long time, except for the grain boundary, which sometimes shows a bright line-shape contrast by SEM images (see Supporting Information Figure S10).

Raman and PL mapping on these WS_2 islands were performed to see the film uniformity, as well as the crystalline nature. Uniform SEM (Figure 4a−d), OM (Figure 4e,h,k,n), Raman (Figure 4f,i,l,o), and PL (Figure 4g,j,m,p) address a rather high thickness uniformity of the typical flakes. Unexpectedly, no clear signs of remarkable PL enhancement[21] or suppression[29] at

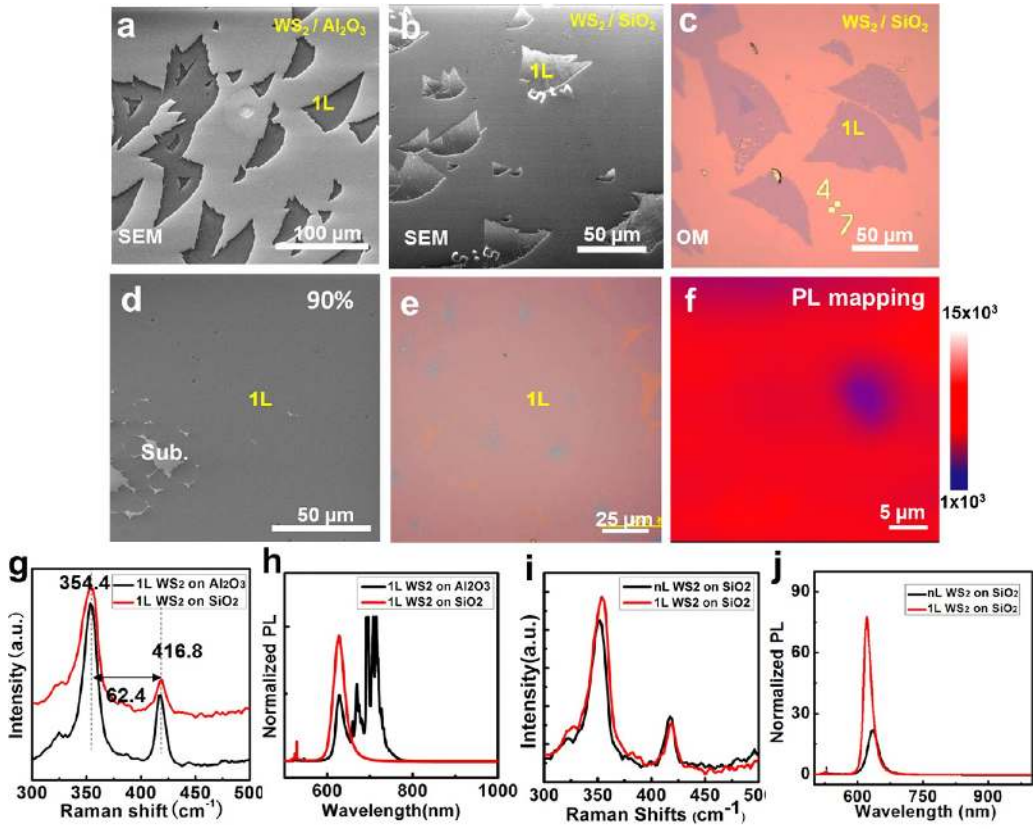

Figure 3. Comparison of morphology and spectroscopy of as-grown and transferred WS_2. (a, b) SEM images of 1L WS_2 flakes before (on sapphire) and after (on SiO_2/Si) transfer, respectively. (c) Corresponding optical images of the sample on SiO_2/Si. (d, e) Nearly a full coverage of monolayer as-grown and transferred WS_2 films. (f) Corresponding PL mapping of excitonic emission integrated from 600 to 700 nm. (g, h) Raman and PL spectra of 1L WS_2 before and after transfer. (i, j) Raman and PL spectra of 1L and nL WS_2 on SiO_2/Si.

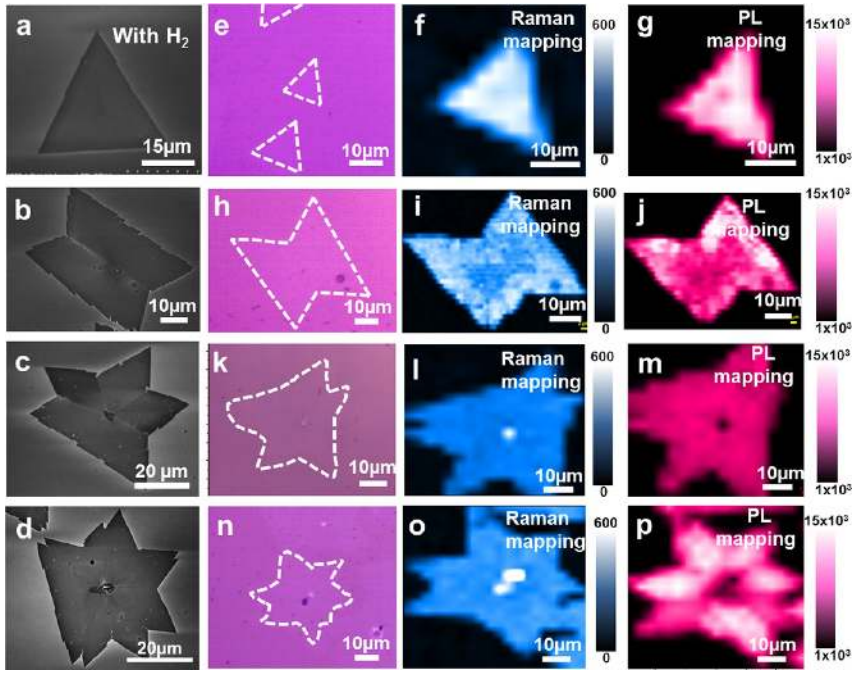

Figure 4. Raman and PL mapping of different shapes of monolayer WS_2 flakes. (a–d) SEM morphologies of monolayer WS_2 flakes. (e, h, k, n) Optical images of WS_2 flakes. (f, i, l, o) Raman mapping of A_{1g} peaks integrated from 400 to 430 cm^{-1} by using a 514 nm excitation laser. (g, j, m, p) PL mapping of A excitonic emission integrated from 600 to 700 nm.

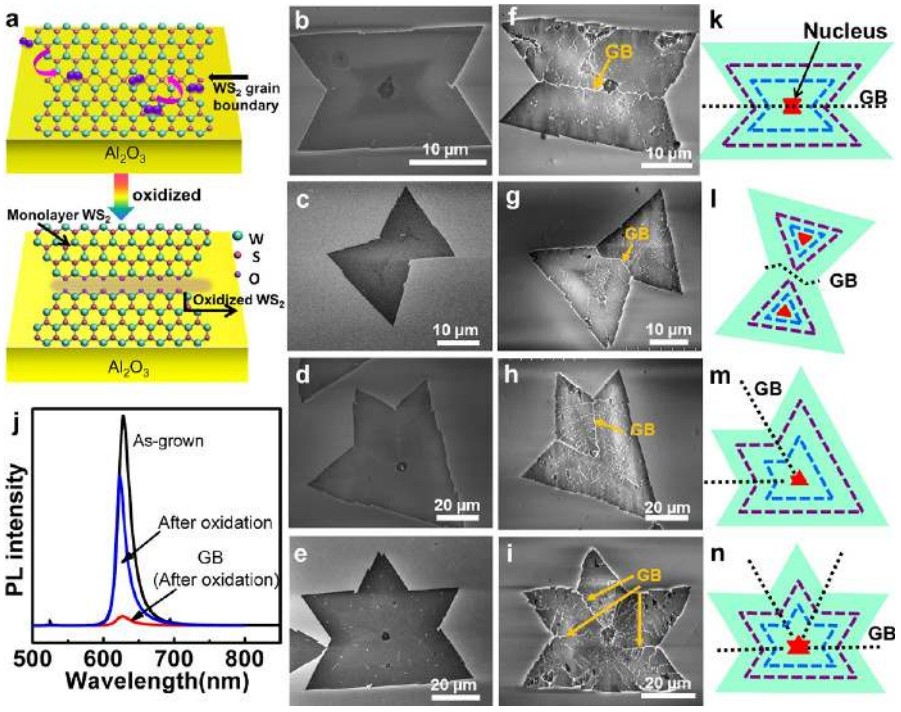

Figure 5. Imaging the grain boundary of WS_2 by mild oxidation under atmospheric conditions. (a) Schematic model of the surface oxidations. (b−e) SEM images of as-grown monolayer WS_2. (f−i) SEM images of WS_2 grain structures after a mild oxidation process. (j) PL spectra of the samples with and without an oxidation process (far away and at the grain boundary). (k−n) Models of the interplay between grain boundary propagation and flake shape evolution for the four typical flakes in b−e.

edges and grain boundaries were found, as reported in prior publications.[19] Hence, the grain boundary of such complicated WS_2 flakes may not be effectively distinguished by the PL mapping data. This may be due to passivation of these sites by impurities in air, which possibly screens or depletes the metallic states at edges and grain boundaries. However, around large defects or nucleation sites, the observed nonuniform Raman and PL intensity is suitable for distinguishing the thicker nucleation sites or obvious defects (Figure 4l,m,o,p).

Unexpectedly, after mild oxidation under moisture-rich ambient conditions (as demonstrated with a schematic model in Figure 5a), the grain boundaries (GBs) of intersecting or joining flakes (Figure 5b−e) could be clearly visualized by SEM, showing bright line shape contrasts (Figure 5f−i). This method has been successfully utilized to identify the grain boundary of graphene due to the oxidation of the underlying Cu.[33,34] For WS_2 on sapphire, the reconstructions at GBs create new states near the Fermi level,[21,30] which may induce a higher reactivity for oxidation or impurity adsorption under the mild oxidation process (for more data see Supporting Information Figure S11). PL measurements were also utilized to characterize the mild surface oxidation, since doping or defects can lead to strong PL quenching or enhancement.[35] As expected, the PL intensity is much reduced on the merging boundary of WS_2 flakes after the oxidation process, as compared with that of the regions far away from the grain boundary and on the as-grown samples (Figure 5j). The Raman intensity and XPS data of WS_2 flakes (with and without oxidation) were also achieved to address the oxidation nature (Supporting Information Figure S12).

This oxidation-induced SEM contrast change was seldom observed on both quasi-triangular WS_2 flakes with crooked boundaries (Figure 1c−e, Figure 2b) (synthesized without H_2 carrier gas) and the regular triangular flakes (synthesized with H_2 carrier gas) with sharp boundaries (Figure 1h), suggestive of their single-crystal nature (see Supporting Information Figures S13, 14).

On the basis of the visualized GBs, the flake growth process could be tracked with the aid of the tentative schematic models in Figure 5k−n (corresponding to Figure 5f−i and b−e), given the grain boundary propagation interplaying closely with flake shape evolution. The dashed lines in Figure 5k−n mark the possible intermediate growth fronts. For the grain structures evolving from merged nuclei (Figure 5k,m,n), GBs propagate linearly, and the resulting flakes resemble the initial shapes of the nuclei. However, for Figure 5l, two solely nucleated domains are suggested to join together, forming a jagged grain boundary.

Note that the schematic views (Figure 5k−n) provide only tentative illustrations of the formation mechanism of the intersecting or joining flakes. Further characterization by dark-field TEM should be useful for identifying the grain boundaries.[29] Anyway, it can be inferred that controlling the initial nucleation shape and the nucleation density is essential for growing large-scale single-crystalline WS_2 films.

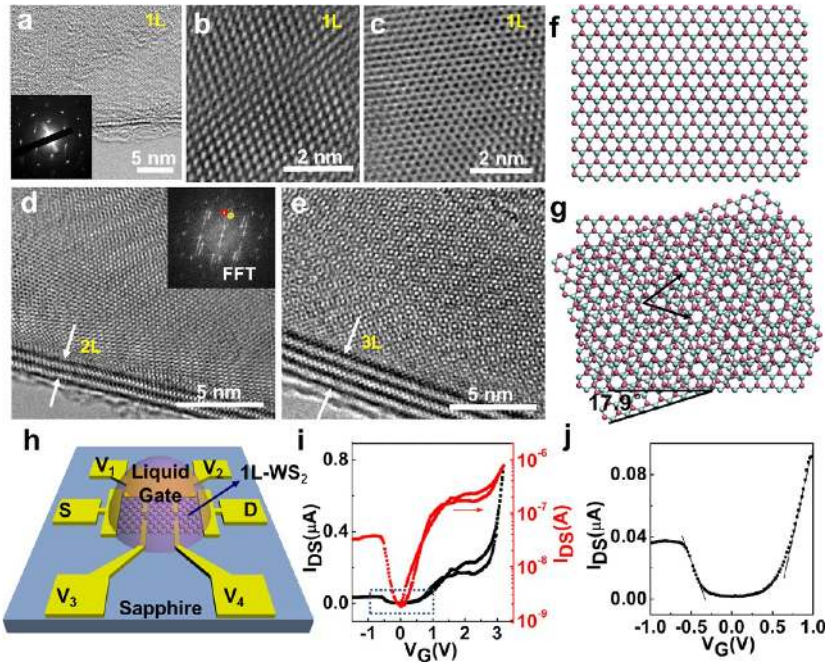

Figure 6. High-resolution transmission electron microscopy (HRTEM) and electrical characterization of WS_2 flakes. (a) TEM image on the edge of a monolayer WS_2 and the SAED pattern (as an inset). (b, c) HRTEM images of monolayer WS_2 with triangular and hexagonal contrasts. (d, e) Atomically resolved images of 2L and 3L WS_2. The arrows indicate the folded edges of the films. The fast Fourier transform image of d is displayed as an inset. (f, g) Atomic models of 1L and 2L WS_2 in c and d, respectively. The arrows in g plot the moiré periodicity. (h) Schematic depiction of the ionic liquid gated FET fabricated with the as-grown monolayer WS_2. (i) Transfer curve of the FET. (j) Zoomed-in plot of the circled region in i.

High-resolution transmission electron microscopy was also utilized to investigate in detail the atomic structures of the transferred WS_2 flakes and their crystal quality. Figure 6a−c show the TEM images of the monolayer WS_2 flake, which exhibit a periodic honeycomb arrangement of the atoms with triangular or hexagonal shaped contrasts. This contrast difference probably arises from the rippling effect of monolayer WS_2[16,36] or the intrinsic contrast difference of W and S atoms.[30] Corresponding selective area electron diffraction (SAED) (200 nm × 200 nm) reveals only one set of diffraction spots, highly suggestive of the single-crystal nature of the monolayer WS_2 sample at large scales. The first-order diffraction spots, corresponding to (100) planes, were used to calculate d (100) equaling ~0.27 nm and a (110) plane with d (110) corresponding to ~0.16 nm. Both interplanar distances coincide well with that of bulk WS_2, again confirming the formation of high-quality WS_2 films.

For thicker WS_2 layers (2L and 3L), the surfaces are characterized with some different moiré patterns in proximity to the folded edges (Figure 6d,e) (see Supporting Information in Figure S15). Corresponding fast Fourier transformation (FFT) analysis of Figure 6d shows two sets of hexagonally arranged spots rotated by ~17.9° to each other, as evidenced from the atomic model in Figure 6g. This addresses a random folding of the few-layer WS_2 after the transfer process.

Electrical measurements were also carried out on as-grown monolayer WS_2 samples to probe their crystal quality. To avoid quality degradation through the transfer process, an ionic liquid was used as the gating dielectric, as schematically shown in Figure 6h. A prominent field-effect modulation was observed to show an on/off ratio of ~10^2 (Figure 6i). The neutral point of the transfer curve is approximately at zero gate voltage, which indicates a low intrinsic doping level in the WS_2 sample. A zoomed-in plot of the black rectangle in Figure 6i exhibits ambipolar behavior of the device (Figure 6j).

The field-effect mobility of the device was extracted by $\mu = (L/WC_iV_D)(dI_D/dV_G)$, where L (30 μm), W (15 μm), and V_G are the channel length, channel width, and gate voltage, respectively. C_i, estimated to be ~10 μF/cm^2, is the area capacitance. With the linear region drawn in Figure 6j, the electron and hole mobilities were deduced to be 0.46 and 0.28 cm^2 V^{-1} s^{-1}, respectively, which is comparable with other CVD-synthesized TMDC monolayers.[20,37]

CONCLUSION

In conclusion, we have synthesized large-area and high-quality WS_2 layers on sapphire, with thickness variable from monolayer to multilayers and domain size up to ~50 μm. By using a carrier gas mixture of H_2 and Ar, we can achieve nearly triangular and intersecting or joined triangular shaped monolayer WS_2 flakes.

Through a mild oxidation process, we can identify the domain boundaries of the complicated flakes. The transferability of WS_2 layers onto other arbitrary substrates such as SiO_2/Si makes our LPCVD WS_2 a perfect candidate for engineering a variety of applications in nanoelectronics and optoelectronics.

METHODS

WS_2 Growth and Transfer. The growth was performed inside a multi-temperature-zone tube furnace (Lindberg/Blue M) equipped with a 1-in.-diameter quartz tube. Sulfur powder was placed outside the hot zone and mildly sublimated at ~100 °C. WO_3 powder (Alfa Aesar, purity 99.9%) and sapphire substrates (⟨0001⟩ oriented single crystals) were successively placed inside the hot center. Argon (flow rate 80 sccm) (or mixed Ar and H_2 gas with flow rates of 80 and 10 sccm) was used to convey WO_{3-x} vapor species to the downstream substrates. The growth pressure was set at 30 Pa with a growth temperature at ~900 °C and growth time of ~60 min. The as-grown WS_2 sample can be transferred onto arbitrary substrates with a commonly used method.[19] The backside Al_2O_3 was etched by a concentrated NaOH solution.

Characterization of Monolayer and Few-Layer WS_2. Optical microscopy (Olympus DX51), Raman spectroscopy (Horiba, LabRAM HR-800), AFM (Vecco Nanoscope IIIa), SEM (Hitachi S-4800; acceleration voltage, 5−30 kV), and TEM (JEOL JEM-2100F LaB6; acceleration voltage, 200 kV) were used to characterize the sample. A carbon film supported on copper grids was used for TEM characterization. The mild oxidation process was executed by heating as-grown samples under moisture-rich ambient conditions (humidity ~60%) for 10 min at 80 °C.

Mobility Measurements of Monolayer WS_2 with Ionic Liquid Gating. The WS_2 flake was patterned by e-beam lithography into a Hall bar with the dimensions of ~30 μm (channel length) × 15 μm (width). *N,N*-Diethyl-*N*-(2-methoxyethyl)-*N*-methylammonium bis(trifluoromethylsulfonyl)imide (from Kanto Chemical Co.) was used as the liquid gate. Note that the counter gate electrode was designed to have a much larger surface area than that of the channel material so that the EDL capacitance formed at the channel surface would be the dominant contribution. All transportation characteristics of the EDL transistors were measured with a V_G sweep speed of 20 mV s^{-1} under high-vacuum mode inside a Quantum Design PPMS.[38−40]

Conflict of Interest: The authors declare no competing financial interest.

Acknowledgment. This work was financially supported by the National Natural Science Foundation of China (Grants Nos. 51222201, 51290272, 21073003, 21201012, 51121091, 51072004) and the Ministry of Science and Technology of China (Grants Nos. 2011CB921903, 2012CB921404, 2012CB933404, 2013CB932603, 2011CB933003). H.T.Y., Y.C., and H.Y.H. acknowledge support by the U.S. Department of Energy, Office of Basic Energy Sciences, Materials Sciences and Engineering Division, under Contract DE-AC02-76SF00515.

Supporting Information Available: The crystalline structure of sapphire, SEM images of WS_2 prepared without and with H_2, SEM images of as-grown WS_2 at different growth temperatures and D_{ss}, details of the full-coverage WS_2 layers, supplementary AFM characterization of WS_2 nanosheets, PL property of sapphire, SEM images of intersecting or joining monolayer WS_2 flakes, and TEM and XPS data of WS_2. This material is available free of charge *via* the Internet at http://pubs.acs.org.

REFERENCES AND NOTES

1. Novoselov, K. S.; Jiang, D.; Schedin, F.; Booth, T. J.; Khotkevich, V. V.; Morozov, S. V.; Geim, A. K. Two-Dimensional Atomic Crystals. *Proc. Natl. Acad. Sci. U.S.A.* **2005**, *102*, 10451–10453.
2. Butler, S. Z.; Hollen, S. M.; Cao, L.; Cui, Y.; Gupta, J. A.; Gutiérrez, H. R.; Heinz, T. F.; Hong, S. S.; Huang, J.; Ismach, A. F.; *et al*. Progress, Challenges, and Opportunities in Two-Dimensional Materials beyond Graphene. *ACS Nano* **2013**, *7*, 2898–2926.
3. Geim, A. K.; Novoselov, K. S. The Rise of Graphene. *Nat. Mater.* **2007**, *6*, 183–191.
4. Wang, Q. H.; Kalantar-Zadeh, K.; Kis, A.; Coleman, J. N.; Strano, M. S. Electronics and Optoelectronics of Two-Dimensional Transition Metal Dichalcogenides. *Nat. Nanotechnol.* **2012**, *7*, 699–712.
5. Chhowalla, M.; Shin, H. S.; Eda, G.; Li, L.-J.; Loh, K. P.; Zhang, H. The Chemistry of Two-Dimensional Layered Transition Metal Dichalcogenide Nanosheets. *Nat. Chem.* **2013**, *5*, 263–275.
6. Huang, X.; Zeng, Z.; Zhang, H. Metal Dichalcogenide Nanosheets: Preparation, Properties and Applications. *Chem. Soc. Rev.* **2013**, *42*, 1934–1946.
7. Zhao, W.; Ghorannevis, Z.; Chu, L.; Toh, M.; Kloc, C.; Tan, P.; Eda, G. Evolution of Electronic Structure in Atomically Thin Sheets of WS_2 and WSe_2. *ACS Nano* **2013**, *7*, 791–797.
8. Zeng, H.; Liu, G.-B.; Dai, J.; Yan, Y.; Zhu, B.; He, R.; Xie, L.; Xu, S.; Chen, X.; Yao, W. Optical Signature of Symmetry Variations and Spin-Valley Coupling in Atomically Thin Tungsten Dichalcogenides. *Sci. Rep.* **2013**, *3*, 1608.
9. Shi, H.; Pan, H.; Zhang, Y.-W.; Yakobson, B. I. Quasiparticle Band Structures and Optical Properties of Strained Monolayer MoS_2 and WS_2. *Phys. Rev. B* **2013**, *87*, 155304.
10. Kośmider, K.; Fernández-Rossier, J. Electronic Properties of the MoS_2-WS_2 Heterojunction. *Phys. Rev. B* **2013**, *87*, 075451.
11. Georgiou, T.; Jalil, R.; Belle, B. D.; Britnell, L.; Gorbachev, R. V.; Morozov, S. V.; Kim, Y.-J.; Gholinia, A.; Haigh, S. J.; Makarovsky, O. Vertical Field-Effect Transistor Based on Graphene-WS_2 Heterostructures for Flexible and Transparent Electronics. *Nat. Nanotechnol.* **2012**, *8*, 100–103.
12. Britnell, L.; Ribeiro, R.; Eckmann, A.; Jalil, R.; Belle, B.; Mishchenko, A.; Kim, Y.; Gorbachev, R.; Georgiou, T.; Morozov, S. Strong Light-Matter Interactions in Heterostructures of Atomically Thin Films. *Science* **2013**, *340*, 1311–1314.
13. Zeng, Z.; Yin, Z.; Huang, X.; Li, H.; He, Q.; Lu, G.; Boey, F.; Zhang, H. Single-Layer Semiconducting Nanosheets: High-Yield Preparation and Device Fabrication. *Angew. Chem., Int. Ed.* **2011**, *50*, 11093–11097.
14. Voiry, D.; Yamaguchi, H.; Li, J.; Silva, R.; Alves, D. C.; Fujita, T.; Chen, M.; Asefa, T.; Shenoy, V.; Eda, G. Enhanced Catalytic Activity in Strained Chemically Exfoliated WS_2 Nanosheets for Hydrogen Evolution. *Nat. Mater.* **2013**, *12*, 850–855.
15. Ramakrishna Matte, H.; Gomathi, A.; Manna, A. K.; Late, D. J.; Datta, R.; Pati, S. K.; Rao, C. MoS_2 and WS_2 Analogues of Graphene. *Angew. Chem., Int. Ed.* **2010**, *122*, 4153–4156.
16. Coleman, J. N.; Lotya, M.; O'Neill, A.; Bergin, S. D.; King, P. J.; Khan, U.; Young, K.; Gaucher, A.; De, S.; Smith, R. J.; *et al*. Two-Dimensional Nanosheets Produced by Liquid Exfoliation of Layered Materials. *Science* **2011**, *331*, 568–571.
17. Wang, Y.; Zhou, C.; Wang, W.; Zhao, Y. Preparation of Two Dimensional Atomic Crystals-BN, WS_2 and MoS_2 by Supercritical CO_2 Assisted with Ultrasonic. *Ind. Eng. Chem. Res.* **2013**, *52*, 4379–4382.
18. Sik Hwang, W.; Remskar, M.; Yan, R.; Protasenko, V.; Tahy, K.; Doo Chae, S.; Zhao, P.; Konar, A.; Seabaugh, A.; Jena, D. Transistors with Chemically Synthesized Layered Semiconductor WS_2 Exhibiting 10^5 Room Temperature Modulation and Ambipolar Behavior. *Appl. Phys. Lett.* **2012**, *101*, 013107.
19. Lee, Y.-H.; Yu, L.; Wang, H.; Fang, W.; Ling, X.; Shi, Y.; Lin, C.-T.; Huang, J.-K.; Chang, M.-T.; Chang, C.-S. Synthesis and Transfer of Single Layer Transition Metal Disulfides on Diverse Surfaces. *Nano Lett.* **2013**, *13*, 1852–1857.

20. Lee, Y. H.; Zhang, X. Q.; Zhang, W.; Chang, M. T.; Lin, C. T.; Chang, K. D.; Yu, Y. C.; Wang, J. T. W.; Chang, C. S.; Li, L. J. Synthesis of Large-Area MoS_2 Atomic Layers with Chemical Vapor Deposition. *Adv. Mater.* **2012**, *24*, 2320–2325.
21. Gutiérrez, H. R.; Perea-López, N.; Elías, A. L.; Berkdemir, A.; Wang, B.; Lv, R.; López-Urías, F.; Crespi, V. H.; Terrones, H.; Terrones, M. Extraordinary Room-Temperature Photoluminescence in Triangular WS_2 Monolayers. *Nano Lett.* **2013**, *13*, 3447–3454.
22. Berkdemir, A.; Gutiérrez, H. R.; Botello-Méndez, A. R.; Perea-López, N.; Elías, A. L.; Chia, C.-I.; Wang, B.; Crespi, V. H.; López-Urías, F.; Charlier, J.-C. Identification of Individual and Few Layers of WS_2 Using Raman Spectroscopy. *Sci. Rep.* **2013**, *3*, 1755.
23. Britnell, L.; Gorbachev, R.; Jalil, R.; Belle, B.; Schedin, F.; Mishchenko, A.; Georgiou, T.; Katsnelson, M.; Eaves, L.; Morozov, S. Field-Effect Tunneling Transistor Based on Vertical Graphene Heterostructures. *Science* **2012**, *335*, 947–950.
24. Yin, Z.; Li, H.; Li, H.; Jiang, L.; Shi, Y.; Sun, Y.; Lu, G.; Zhang, Q.; Chen, X.; Zhang, H. Single-Layer MoS_2 Phototransistors. *ACS Nano* **2012**, *6*, 74–80.
25. Nie, S.; Wofford, J. M.; Bartelt, N. C.; Dubon, O. D.; McCarty, K. F. Origin of the Mosaicity in Graphene Grown on Cu (111). *Phys. Rev. B* **2011**, *84*, 155425.
26. Huang, J.-K.; Pu, J.; Chuu, C.-P.; Hsu, C.-L.; Chiu, M.-H.; Juang, Z.-Y.; Chang, Y.-H.; Chang, W.-H.; Iwasa, Y.; Chou, M.-Y. Large-Area and Highly Crystalline WSe_2 Monolayers: from Synthesis to Device Applications. Preprint at http://arxiv.org/abs/1304.7365.
27. Loginova, E.; Bartelt, N. C.; Feibelman, P. J.; McCarty, K. F. Evidence for Graphene Growth by C Cluster Attachment. *New J. Phys.* **2008**, *10*, 093026.
28. Lauritsen, J. V.; Kibsgaard, J.; Helveg, S.; Topsøe, H.; Clausen, B. S.; Lægsgaard, E.; Besenbacher, F. Size-Dependent Structure of MoS_2 Nanocrystals. *Nat. Nanotechnol.* **2007**, *2*, 53–58.
29. van der Zande, A. M.; Huang, P. Y.; Chenet, D. A.; Berkelbach, T. C.; You, Y.; Lee, G.-H.; Heinz, T. F.; Reichman, D. R.; Muller, D. A.; Hone, J. C. Grains and Grain Boundaries in Highly Crystalline Monolayer Molybdenum Disulphide. *Nat. Mater.* **2013**, *12*, 554–561.
30. Zhou, W.; Zou, X.; Najmaei, S.; Liu, Z.; Shi, Y.; Kong, J.; Lou, J.; Ajayan, P. M.; Yakobson, B. I.; Idrobo, J.-C. Intrinsic Structural Defects in Monolayer Molybdenum Disulfide. *Nano Lett.* **2013**, *13*, 2615–2622.
31. Najmaei, S.; Liu, Z.; Zhou, W.; Zou, X.; Shi, G.; Lei, S.; Yakobson, B. I.; Idrobo, J.-C.; Ajayan, P. M.; Lou, J. Vapour Phase Growth and Grain Boundary Structure of Molybdenum Disulphide Atomic Layers. *Nat. Mater.* **2013**, *12*, 754–759.
32. Elías, A. L.; Perea-López, N.; Castro-Beltrán, A.; Berkdemir, A.; Lv, R.; Feng, S.; Long, A. D.; Hayashi, T.; Kim, Y. A.; Endo, M. Controlled Synthesis and Transfer of Large Area WS_2 Sheets: From Single-Layer to Few-Layers. *ACS Nano* **2013**, *7*, 5235–5242.
33. Li, X. S.; Cai, W. W.; An, J.; Kim, S.; Nah, J.; Yang, D. X.; Piner, R.; Velamakanni, A.; Jung, I.; Rouff, R. S.; *et al*. Large-Area Synthesis of High-Quality and Uniform Graphene Films on Copper Foils. *Science* **2009**, *324*, 1312–1314.
34. Duong, D. L.; Han, G. H.; Lee, S. M.; Gunes, F.; Kim, E. S.; Kim, S. T.; Kim, H.; Ta, Q. H.; Choi, J. Y.; Lee, Y. H.; *et al*. Probing Graphene Grain Boundaries with Optical Microscopy. *Nature* **2012**, *490*, 235–239.
35. Mak, K. F.; He, K. L.; Lee, C. G.; Lee, G. H.; Hone, J.; Teinz, T. F.; Shan, J. Tighlty Bound Trions in Monolayer MoS_2. *Nat. Mater.* **2013**, *12*, 207–211.
36. Brivio, J.; Alexander, D. T. L.; Kis, A. Ripples and Layers in Ultrathin MoS_2 Membranes. *Nano Lett.* **2011**, *11*, 5148–5153.
37. Wang, X. S.; Feng, H. B.; Wu, Y. M.; Jiao, L. Y. Controlled Synthesis of Highly Crystalline MoS_2 Flakes by Chemical Vapor Deposition. *J. Am. Chem. Soc.* **2013**, *135*, 5304–5307.
38. Yuan, H. T.; Saeed, M. B.; Morimoto, K.; Shimotani, H.; Nomura, K.; Arita, R.; Kloc, Ch.; Nagaosa, N.; Tokura, Y.; Iwasa, Y. Zeeman-Type Spin Splitting Controlled with an External Electric Field. *Nat. Phys.* **2013**, *9*, 563–569.
39. Chen, Z. Y.; Yuan, H. T.; Zhang, Y. F.; Nomura, K.; Gao, T.; Shimotani, H.; Liu, Z. F.; Iwasa, Y. Spin-Orbit Interaction in Trilayer Graphene Exemplified in Liquid Gated Electric-Double-Layer Transistors. *Nano Lett.* **2012**, *12*, 2212–2216.
40. Yuan, H. T.; Shimotani, H.; Tsukazaki, A.; Ohtomo, A.; Kawasaki, M.; Iwasa, Y. High-Density Carrier Accumulation in ZnO Field-Effect Transistors Gated by Electric Double Layers of Ionic Liquids. *Adv. Funct. Mater.* **2009**, *19*, 1046–1053.